ENTROPY PRODUCTION OF EMERGING TURBULENT SCALES IN A TEMPORAL SUPERCRITICAL N-HEPTANE/NITROGEN THREE-DIMENSIONAL MIXING LAYER

N. Okong'o and J. Bellan†

Jet Propulsion Laboratory, California Institute of Technology, Pasadena, CA. 91109

Word Count: 5882 (introduction 355; model 883; results 1266; conclusions 603; acknowledgment 64; equations 336; tables and figures 2200; references 175)

†Corresponding author: Dr. J. Bellan

Jet Propulsion Laboratory

California Institute of Technology

MS. 125-109

4800 Oak Grove Drive

Pasadena, CA 91109

USA

Tel: (818) 354-6959

Fax: (818) 393-5011

Email: Josette.Bellan@jpl.nasa.gov

Colloquium: Turbulent non-premixed combustion

Oral presentation

ABSTRACT

A study of emerging turbulent scales entropy production is conducted for a supercritical shear layer as a precursor to the eventual modeling of Subgrid Scales (from a turbulent state) leading to Large Eddy Simulations. The entropy equation is first developed for a real, nonideal fluid using a validated all-pressure fluid model, and the entropy flux and production terms are identified. Employing a Direct Numerical Simulation (DNS) created database of a temporal 3D supercritical shear layer using the fluid model, the different contributions to the irreversible entropy production term are evaluated. Both domain averaged and root-mean-square (RMS) terms are computed at three different stages of the DNS, representing the timewise ascending, culmination and descending branches of the spatially averaged positive spanwise vorticity. The unfiltered and filtered databases are compared to evaluate the relative importance of irreversible entropy production from viscous, Fourier heat diffusion and molar fluxes terms. The results show that the average entropy production is dominated by the viscous terms at all stages of the evolution; however, the contribution to the RMS of the molar flux term for both the ascending and descending branches is non-negligible. This latter result is traced to the molar gradients tending to be smeared by emerging turbulent scales. Based on this finding, a physical picture of the layer evolution is presented involving competition between large scales entraining heavy fluid from the lower stream and forming strong density and mass fraction gradients at spatially varying locations with time, and small scale turbulent structures evolving but being damped by contact with the newly formed strong density gradient regions which act similar to material surfaces. Analysis of the results shows that the primary contribution to the molar flux dissipation for both the average and the RMS is the mixture nonideality.

1 Introduction

Numerous combustion systems, such as liquid rocket, gas turbine and diesel engines, operate at supercritical pressures, yet the current understanding of turbulent supercritical flows and sprays is in infancy. The experimental investigation of Brown and Roshko [1] of a high pressure shear layer and the recent observations of fluid jet disintegration under supercritical conditions by Mayer et al. [2], [3], [4] and Chehroudi et al. [5] constitute a scant empirical database for turbulent model validation. Under these circumstances, the approach of Direct Numerical Simulation (DNS) pursued to turbulence transition followed by a Large Eddy Simulation (LES) based upon Subgrid Scale (SGS) models extracted from the analysis of the DNS database can be very helpful for developing a turbulent supercritical fluid model. Mayer and Tamura [2] conclude from their observations that fluids injected in a chamber at supercritical conditions (with respect to the injected fluid) behave very differently from those injected in a subcritical conditions chamber and advise that liquid core and drop tracking modeling approaches using distribution functions are inappropriate to describe phenomena in the supercritical regime. Prior to having this information available, Oefelein and Yang [6] conducted a LES simulation tracking drops in a Lagrangian manner and using the SGS model of Erlebacher et al. [7] derived from subcritical turbulence. The fluid model included real gas equations of state (EOS) and high pressure transport coefficients, but assumed phase equilibrium at a hypothetical material surface, did not include either high pressure solubility or Soret and Dufour effects, and additionally neglected viscous dissipation. The results in [6] highlight the influence of the pressure on the spray evolution. For example, it is found that the coupling between the spray and its surroundings increases with pressure due to the enhanced turbulent diffusion and to the variations in the gas phase structures stemming from changes in composition. Additionally, the LO_x/H_2 simulations showed that both mixing and dispersion become stronger functions of the SGS

fluctuations and of the flowing H_2 large scale coherent structures as p increases, indicating that an accurate, supercritically based SGS model (and we note again that the model in [6] is subcritically based) is crucial to obtaining quantitatively validated predictions. The present study represents a step in this direction.

2 Fluid Model and Governing Equations

The fluid model used in this investigation is based on that developed by Harstad and Bellan [8], [9], [10] and it has been validated [9], [10] for C_7H_{16}/N_2 with Nomura et al.'s [11] microgravity data for the entire range of the data encompassing both the subcritical and supercritical regime. This model has been used by Miller et al. [13] to develop a DNS of a C_7H_{16}/N_2 shear layer where C_7H_{16} is the slower, lower stream fluid. In [13] the simulation was stopped at a nondimensional time of 100 (see definition below) and the focus was on the influence of the thermal diffusion factors on the evolution of the layer and on the specific visual aspects characteristic of the supercritical regime. It is noteworthy that even at this early stage of the layer, visual features were qualitatively similar to those observed by Chehroudi et al. [5] in their experiments in that regions of strong density gradients formed both in the braid and between the braids of the layer; these regions were optically detected as wispy threads emanating from the injected jet. Due to space restrictions, the published model equations will not reproduced here except for the essential equations needed in the present derivation.

2.1 Shear layer model

The temporal shear layer configuration, initial conditions and numerics have been thoroughly documented by Miller and Bellan [12] with the classical nomenclature being adopted for the coordinates

(x_1 streamwise, x_2 crosstream, x_3 spanwise). The compressible form of the conservation equations for a binary mixture of general (Newtonian) fluids are:

$$\partial\rho/\partial t + \partial\left[\rho u_j\right]/\partial x_j = 0, \tag{1}$$

$$\partial\left(\rho u_i\right)/\partial t + \partial\left[\rho u_i u_j + p\delta_{ij} - \sigma_{ij}\right]/\partial x_j = 0, \tag{2}$$

$$\partial\left(\rho e_t\right)/\partial t + \partial\left[\left(\rho e_t + p\right)u_j - u_i\sigma_{ij} + q_{IK,j}\right]/\partial x_j = 0, \tag{3}$$

$$\partial\left(\rho Y_h\right)/\partial t + \partial\left[\rho Y_h\, u_j + J_{hj}\right]/\partial x_j = 0, \tag{4}$$

where ρ is the density, u_i is the velocity, $e_t = e + u_i u_i/2$ is the total energy (i.e. internal energy, e, plus kinetic energy), p is the thermodynamic pressure (the temperature is T) and Y_h is the mass fraction of heptane (the mass fraction of nitrogen is $Y_n = 1 - Y_h$). Furthermore, $\mathbf{q}_{IK}$ is the Irwing - Kirkwood (subscript IK) form of the heat flux vector (see [14] and discussion below), $\mathbf{J}_h$ is the heptane mass flux vector and σ_{ij} is the Newtonian viscous stress tensor

$$\sigma_{ij} = \mu\left[\partial u_i/\partial x_j + \partial u_j/\partial x_i - (2/3)(\partial u_k/\partial x_k)\delta_{ij}\right] \equiv \mu[2S_{ij} - (2/3)S_{kk}\delta_{ij}], \tag{5}$$

where δ_{ij} is the Kronecker delta function, μ is the mixture viscosity which is in general a function of the thermodynamic state variables and S_{ij} and S_{kk} are defined from eq. 5. According to [8] and [10], the form of the diffusional fluxes is:

$$q_{IK,j} = -\left[\lambda'_{IK}\partial T/\partial x_j + \alpha_{IK}R_u T[m/(m_n m_h)]J'_{hj}\right], \tag{6}$$

$$J_{hj} = -\left[J'_{hj} + \alpha_{BK}Y_n Y_h\ \rho D/T\ \partial T/\partial x_j\right], \tag{7}$$

$$J'_{hj} = \rho D\left[\alpha_D\partial Y_h/\partial x_j + Y_n Y_h m_n m_h/(R_u T m)\left(v_{,h}/m_h - v_{,n}/m_n\right)\partial p/\partial x_j\right] \tag{8}$$

where eq. 6 is the Irwing-Kirkwood form of the heat flux ([14]); D is the binary diffusion coefficient; the mass fraction Y is related to the mole fraction, X, by $m_\alpha Y_\alpha = mX_\alpha$ where m_α is the molecular weight of pure species α and the mixture molecular weight is $m = X_n m_n + X_h m_h$; the molar volume

v is related to the density by $v = m/\rho$; $v_{,\alpha}$ is the partial molar volume; α_D is the mass diffusion factor; and λ'_{IK} is a thermal conductivity. Also, α_{IK} and α_{BK} are the thermal diffusion factors corresponding to the IK and the Bearman-Kirkwood (subscript BK) forms of the heat flux ([14]), respectively; they are the new transport coefficients that are introduced by the Soret (in the molar fluxes) and the Dufour (in the heat flux) terms of the transport matrix, and are characteristic of the particular species pairs under consideration. Although currently there is no general information as to the functional form of α_{IK} and α_{BK} with respect to the primary variables (p, T, Y_i) and/or their magnitudes, it was shown [10] that they are related through

$$\alpha_{IK} = \alpha_{BK} + (1/R_u T)(m_n m_h/m)(h_{,h}/m_h - h_{,n}/m_n) \tag{9}$$

where $h_{,\alpha}$ is the partial molar enthalpy, and furthermore Harstad and Bellan [20] were able to determine an approximate $\alpha_{BK}(p, T, Y_i)$ functional form for C_7H_{16}/N_2 through comparisons with part of the data in [11]. Moreover, Harstad and Bellan [10] have shown that λ'_{IK} does not correspond to the kinetic theory (subscript KT) definition of the thermal conductivity in that $\lim_{p\to 0} \lambda'_{IK} \neq \lambda_{KT}$, but it is related to the thermal conductivity, λ, through $\lambda'_{IK} = \lambda + X_n X_h\ \alpha_{IK}\ \alpha_{BK} R_u \rho D/m$,where $\lim_{p\to 0} \lambda = \lambda_{KT}$. To calculate $\alpha_D = 1 + X_\alpha[\partial \ln(\varphi_\alpha)/\partial X_\alpha]$, the fugacity coefficients, φ_α, are calculated from the EOS. The Peng-Robinson EOS is employed in conjunction with the above equations, yielding $< 1\%$ error over highly accurate EOSs, and D and λ are calculated for the high (p, T) regime as in [8]. A reference μ, μ_r, is obtained from the specified initial Reynolds number, Re_0, and further used to calculate $\mu(T)$ [13].

2.2 Entropy equation

The entropy of a fluid within a region may change due to both reversible flux of entropy through the fluid boundary, and through irreversible entropy production [15]. The irreversible entropy

production is the dissipation and it is inherently important in systems undergoing production of turbulent scales. For example, Liu et al. [16] have evaluated the subgrid energy dissipation to document the level of isotropy during rapid straining to turbulence and used it as an indicator for developing SGS models. To understand the evolution of the layer, our focus is on the total irreversible entropy.

Following Hirshfelder et al. [15], the entropy equation is

$$\rho Ds/Dt \equiv \partial(\rho s)/\partial t + \partial(\rho s u_j)/\partial x_j = -\partial \Sigma_j/\partial x_j + g \tag{10}$$

where s is the entropy per unit mass, Σ_j represents the reversible flux of entropy, g is the rate of irreversible entropy production and D/Dt is the substantial derivative. On the other hand, the differential thermodynamic expression of s yields

$$TDs/Dt = De/Dt + pD(1/\rho)/Dt - \mu_h D[n_h/(\rho N_A)]/Dt - \mu_n D[n_n/(\rho N_A)]/Dt \tag{11}$$

where μ_n and μ_h are the chemical potentials (partial molar Gibbs free energy), $n_\alpha = \rho Y_\alpha N_A/m_\alpha$ and N_A is the Avogadro number. By replacing the substantial derivatives on the right hand side of eq. 11 with the expressions from eqs. 1-4 and comparing the resulting equation with eq. 10 one identifies Σ_j and g

$$\Sigma_j = \left(q_{IK,j} - \mu_n J_{hj}/m_h - \mu_n J_{nj}/m_n\right)/T \tag{12}$$

$$g = \sigma_{ij}(\partial u_i/\partial x_j)/T - q_{IK,j}(\partial T/\partial x_j)/T^2 - (J_{hj}/m_h)\partial(\mu_h/T)/\partial x_j - (J_{nj}/m_n)\partial(\mu_n/T)/\partial x_j \tag{13}$$

where $J_{nj} = -J_{hj}$. Calculating $\partial(\mu_\alpha/T)/\partial x_j$ from thermodynamics and replacing in eq. 13 one finds

$$g = \mu\left(2S_{ij}S_{ij} - \tfrac{2}{3}S_{kk}S_{ll}\right)/T + \lambda(\partial T/\partial x_j)(\partial T/\partial x_j)/T^2 + (R_u m J_{hj} J_{hj})/(Y_n Y_h \rho D m_n m_h) \tag{14}$$

where $(\sigma_{ij}/T)\partial u_i/\partial x_j$ was rewritten as a function of S_{ij}. Note that the irreversible entropy expression eq. 14 is expectably quadratic; it states that g is the sum of viscous, Fourier heat flux and

molar flux contributions

$$g = g_{vis} + g_{temp} + g_{mass} \tag{15}$$

$$g_{vis} = \frac{\mu}{T}\left(2S_{ij}S_{ij} - \tfrac{2}{3}S_{kk}S_{ll}\right), \quad g_{temp} = \frac{\lambda}{T^2}\frac{\partial T}{\partial x_j}\frac{\partial T}{\partial x_j}, \quad g_{mass} = \frac{1}{Y_n Y_h \rho D}\frac{R_u m}{m_n m_h} J_{hj} J_{hj} \tag{16}$$

where according to eqs. 7-8 g_{mass} contains the departure from mixture nonideality, $\propto \alpha_D$, and the Soret term, $\propto \alpha_{BK}$. The question arises as to the importance of each one of these contributions at various stages of the supercritical shear layer evolution and the implication that this has upon transition, or lack of transition, to turbulence.

3 Results and Discussion

The database used to perform the analysis is from a 3D temporal supercritical shear layer DNS. For these simulations, Re_0 based on the initial vorticity thickness, $\delta_{\omega,0}$, and on the velocity difference across the mixing layer, $\Delta U_0 = U_1 - U_2$, was 400, the initial Mach number was 0.4, the upper faster stream (subscript 1) was initially pure nitrogen while stream 2 was initially pure heptane with temperatures $T_1 = 1000K$ and $T_2 = 600K$, respectively, $(\rho_2/\rho_1)_0 = 12.88$ and $p_0 = 60atm$. The grid has 200×232×120 points, and measures 0.2m×0.232m×0.12m. The initial velocity profile, amplitudes of the forcing perturbations and boundary conditions are all discussed in detail in [12]. Consistent with the validated results in [10], $\alpha_{IK} = 0.1$.

3.1 Layer global evolution

Figure 1 illustrates the nondimensionalized momentum thickness $\delta_m/\delta_{\omega,0}$ and product thickness $\delta_p/\delta_{p,0}$ (both calculated as in [13]), the averaged positive spanwise vorticity and the enstrophy as a function of the dimensionless time $t^* = t\Delta U/\delta_{\omega,0}$ to indicate the layer growth and possible transition to turbulence. Due to the initial velocity profile, the spanwise vorticity is initially negative, and the

creation of positive spanwise vorticity indicates the formation of turbulence scales. All of the Fig. 1 curves indicate the formation of small turbulent scales culminating and being eventually damped; the momentum based Reynolds number, $\mathrm{Re}_m \equiv \rho \Delta U \delta_m / \mu = 1080$ at the culmination point of the averaged positive spanwise vorticity (and 1090 at the culmination of $\delta_m/\delta_{\omega,0}$). Although the streamwise vorticity, ω_1, displays the 'mushroom' type features characteristic of 3D scales, the 'collapse' parameter [19] is modest (maximum ~ 7), indicating that transition has not occurred. Physically, entrainment and growth promote the evolution of the turbulent scales, albeit this occurs here slowly compared to a subcritical shear layer [12] due to the large density stratification. However, even once this process is underway, a sustained layer growth and transition to turbulence are not insured; the reason for this is the development of strong $\nabla\rho$ regions which act as material interfaces and damp the turbulence ([17], [18]). Since the layer growth depends primarily on entrainment, and since it is this accelerated growth that promotes the appearance and evolution of the small turbulent scales, this damping mechanism may be enhancing the effect of density stratification. The long time behavior (Fig. 1) is nevertheless puzzling since one would expect that once the turbulence scales dampen the density gradients, transition to turbulence would proceed unopposed as mixing will dominate entrainment. In fact $\delta_p/\delta_{p,0}$, which measures local mixing, quantifying the effectiveness of the small scale processes and the changes in the local distribution of the species, displays a sustained growth, albeit at a slower rate after the culmination of $\delta_m/\delta_{\omega,0}$ and of the averaged positive spanwise vorticity, indicating that local mixing still proceeds at an increased pace. Considering the positive information indicating potential transition to turbulence and the spatial growth of the layer (see below), its decay is surprising. The results below provide an explanation for this behavior.

3.2 Small scale irreversible entropy production

The entropy contribution of the small turbulent scales is the difference between that of the DNS (i.e. unfiltered) and that of the filtered flow field; here the filtered flow field is obtained using a cubic top-hat filter with a filter width of $4\max(\Delta x_1, \Delta x_2, \Delta x_3)$. The magnitude of the three terms for the unfiltered and filtered flow fields is presented in Tables 1 for the average and 2 for the RMS at $t^* = 100, 145$ (culmination of the global positive spanwise vorticity magnitude) and 170. Comparing the various contributions (Table 1 and Fig. 2), one notes that the most important contribution to the average dissipation is from g_{vis} and that the small scales contribute about 25% to g_{vis} (this number and the following % may be filter size dependent) at all times. The contribution to the total dissipation from g_{mass} is two orders of magnitude smaller than the viscous one and the small scales contribute 24%, 22% and 30%, respectively, to g_{mass} at the three times. The contribution of g_{temp} is negligible, being three orders of magnitude smaller than the viscous terms and the participation of the corresponding small scales to g_{temp} is $O(10^{-2})$ at all times. The minute contribution of the small heat flux scales to the heat flux dissipation is totally consistent with the enhanced λ magnitude at supercritical conditions and the finding that the T profile always relaxes first (before ρ and Y_α) under these circumstances [8] because of the enhanced effective Lewis number [20].

A somewhat different picture emerges when analyzing the RMS entropy production (Table 2 and Fig.3), although g_{vis} still dominates and g_{temp} is also negligible at all times. Simple calculations of differences show that the viscous small scales contribute $\sim$ 30% of the g_{vis} RMS at all times whereas the g_{mass} small scales contribute 47%, 29% and 79% of the g_{mass} RMS. Moreover, while the small scales of the g_{mass} RMS contribute $O(10^{-1})$ and $O(10^{-2})$ at $t^* = 100$ and 145, respectively, to the g RMS, at $t^* = 170$ their participation is 12% and therefore non-negligible. To understand the

augmentation of the small scales g_{mass} RMS, braid and between braid contour plots of g, g_{vis}, g_{temp} and g_{mass}were all analyzed; due to space constraints only the braid plot of g at $t^* = 170$ is shown in Fig. 4a . For all three terms, the most important contributions (not shown) occur at locations of the largest $\mid \nabla\rho \mid$ depicted in Fig. 4b at $t^* = 170$, corresponding also to the location of the largest mass fraction gradients ([13]). However, these locations change with time (not shown) and the maximum value of $\mid \nabla\rho \mid$ in the domain is reduced at $t^* = 145$. Therefore, the emerging physical picture is as follows: Entrainment of the lower stream, heavier fluid produces regions of high $\mid \nabla\rho \mid$ while mixing (which is limited by either small scale processes or by the entrainment rate) is initiated. As the turbulent scales appear, they smoothen $\nabla\rho$, thereby reducing the g_{mass} RMS and minimizing it at $t^* = 145$. Further entrainment from the lower stream produces again strong density gradients, but at different locations, resulting in the increase of g_{mass} RMS. Therefore, the behavior of the layer is the direct consequence of the two competing processes of entrainment producing strong density gradients (a stabilizing effect) and mixing reducing the density gradients (a destabilizing effect).

To understand which of the six terms in $J_{hj}J_{hj}$ govern the magnitude of g_{mass}, plane averages were plotted as a function of $x_2/\delta_{\omega,0}$ for both the average and the RMS at the three chosen times (not shown). The results are similar at all times in that the $(\nabla p)^2$ term is negligible and so are the two cross terms containing ∇p. The nonideality (molar diffusion) term is the principal contributor to g_{mass} everywhere except in the nitrogen side of the layer where the cross term between Soret and molar diffusion ($\propto \nabla Y \nabla T$) is of the same magnitude; at other crosstream locations the $\nabla Y \nabla T$ cross term is $\sim 40\%$ of the nonideality term at $t^* = 100$ and its contribution decreases to become practically negligible at $t^* = 170$. The quadratic Soret term ($\propto \nabla T \nabla T$) is small but non-negligible compared to the molar diffusion term ($\sim 15\%$) at $t^* = 100$, however, it becomes insignificant at $t^* = 170$. These features are consistent with the magnitude of g_{temp} and with previous results [8] showing the rapid relaxation of the ∇T terms. Plots of the similar RMS terms exhibit a dominant

contribution from the term $\nabla Y \nabla Y$ followed by the crossterm $\nabla Y \nabla T$ and finally by the $\nabla T \nabla T$ term. Large peaks of the $\nabla Y \nabla Y$ term at both $t^* = 100$ and 170 correspond to regions of density gradients whereas no such peaks are found at $t^* = 145$. Since no peaks are displayed by the $\nabla Y \nabla T$ or the $\nabla T \nabla T$ term, this shows decisively that the g_{mass} RMS correlates with $\mid \nabla \rho \mid$. The physical picture emerging from this comparison is the foremost importance of non ideality in the g_{mass} which is however not dominant when the layer grows and culminates, but governs during its decay. The Soret term is a non-negligible productor of average dissipation through the molar diffusion crossterm and the quadratic term during growth and at culmination but becomes unimportant during decay whereas it's participation to the RMS is insignificant. However, since α_D decreases as the critical point is approached and is null at the critical point, if the mixture is locally near the critical point, the Soret term will be more important at those localities.

4 Conclusions

The focus of this study was the calculation of the irreversible entropy production, i.e. of the dissipation, of emerging small scales in a supercritical shear layer. This work was motivated by the eventual goal of deriving SGS models using a DNS database representing transition to turbulence; indeed one of the main goals of the DNS/SGS/LES protocol is to embed into the SGS the correct small scale behavior which is portrayed by the dissipation. A methodology for exploring this essential aspect of the small scales has thus been developed by first deriving the entropy equation for a real fluid with mixture nonideality, and then identifying the source terms of this equation with either the reversible flux of entropy or the irreversible entropy production. The irreversible contribution was then calculated using a database from a DNS of a temporal supercritical shear layer conducted with a validated fluid model.

For the conditions of this DNS, the layer did not reach a transition state, although the momentum thickness and the averaged positive spanwise vorticity both exhibited regions of sustained growth and the product thickness continued ascending; the momentum based Reynolds number at the culmination point of the averaged positive spanwise vorticity was 1080. Past this culmination point, the layer weakens and the reasons for this are explained using calculations of the irreversible entropy production. These results show that although the average dissipation is dominated by the viscous contribution, the RMS is dominated by the molar dissipation before and after transition and by the viscous dissipation at transition. The reasons for this are unraveled by comparing the regions of strong dissipation with those of significant density and mass fraction gradients. From this comparison, the evolution of the shear layer appears to be the result of the competition between entrainment which creates regions of strong density gradients while also promoting the formation of small turbulent scales, and the small scales which once evolved proceed to smoothen gradients while being themselves damped by evolving new gradients at other locations. To understand which fundamental physical phenomena are responsible for the dissipation, a detailed assessment of the contribution of various terms was made both for the average and the RMS. The results show that for the conditions of the calculation the major participation to the average dissipation is from the viscous term and that the small scales contribute about 25% of the viscous dissipation. The molar fluxes contribution is two orders of magnitude smaller than the viscous one followed by that of the heat flux terms. The principal contribution to the RMS is also due to the viscous dissipation, however, the most active small scales with respect to the corresponding part of the dissipation are those associated with the molar flux away from the culmination of the positive averaged spanwise vorticity. Moreover, the molar fluxes RMS small scales progressively become more important contributors of the total RMS dissipation during the layer evolution. The primary contribution to the RMS molar flux dissipation is due to the quadratic molar diffusion terms,

followed by the Soret crossterm with the molar diffusion. Although the quadratic Soret term is small by comparison with the first two terms, its contribution becomes progressively more important as conditions are closer to the critical point. Finally, all terms proportional to pressure gradients are negligible.

Since both mixture nonideality and Soret effects are non-negligible contributors to the dissipation RMS under supercritcal conditions, and since it was previously concluded that both mixing and dispersion become stronger functions of the SGS fluctuations with increasing pressure [6], this highlights the importance of both of these effects in the modeling of supercritical turbulent flows.

ACKNOWLEDGMENT

add caltech

This study was conducted at the Jet Propulsion Laboratory, and sponsored jointly by the Air Force Office of Scientific Research under the direction of Dr. Julian Tishkoff and by the Army Research Office under the direction of Dr. David Mann under an interagency agreement with NASA. The authors would like to thank Dr. Kenneth G. Harstad of the Jet Propulsion Laboratory for helpful discussions.

spell out

References

[1] Brown, G. L. and Roshko, A.,*J. Fluid Mech.,* 64(4), 775-816, 1974

[2] Mayer, W. and Tamura, H., *Journal of Propulsion and Power*, 12(6), 1137-1147, 1996

[3] Mayer, W., Schick, A., Schweitzer, C. and Schäffler, M., AIAA 96-2620, AIAA/SAE/ ASME/ASEE 32^{nd} Joint Propulsion Conference, 1996

[4] Mayer, W., Ivancic, B., Schik, A. and Hornung, U., AIAA 98-3685, 34^{th} AIAA/ASME/ SAE/ASEE Propulsion Conference, 1998

[5] Chehroudi, B., Talley, D. and Coy, E., AIAA 99-0206, 37^{th} Aerospace Sciences Meeting, 1999

[6] Oefelein, J. C. and Yang, V., AIAA 96-0085, 34^{th} Aerospace Sciences Meeting, 1996

[7] Erlebacher, G., Hussaini, M. Y., Speziale, C. G. and Zang, T. A,. *J. Fluid Mech.*, 238, 155-185, 1992

[8] Harstad, K. and Bellan, J., *Int. J. Heat Mass Transfer,* **41**, 3537-3550, 1998

[9] Harstad, K. and Bellan, J., AIAA 99-206, Joint AIAA/ASME/SAE Propulsion Meeting, 1999

[10] Harstad, K. and Bellan, J., An all-pressure fluid drop model applied to a binary mixture: heptane in nitrogen, accepted for publication in *Int. J. of Multiphase Flow*, 1999

[11] Nomura, H., Ujiie, Y., Rath, H. J., Sato, J. and Kono, M., *26^{th} Symp. (Int.) on Comb.*, 1267-1273, 1996

[12] Miller, R. S. and Bellan, J., *J. Fluid Mech.* **384**, 293-338, 1999

[13] Miller, R. S., Harstad, K. and J. Bellan, J., Direct numerical simulations of supercritical fluid mixing layers applied to heptane nitrogen, submitted for publication to *J. Fluid Mech.*, 1999

[14] Sarman, S. and Evans, D. J.,*Phys. Rev.* **A45**(4), 2370-2379, 1992

[15] Hirshfelder, J. O., Curtis, C. F. and Bird, R. B., *Molecular Theory of Gases and Liquids*, John Wiley and Sons, Inc., 1964

[16] Liu, S., Katz, J. and Meneveau, C., *J. Fluid Mech.*, 387, 281-320, 1999

[17] Hannoun, I. A., Fernando, H. J. S. and List, E. J., *J. Fluid Mech.* **189**, 189-209, 1988

[18] Briggs, D. A., Ferziger, J. H., Koseff, J. R. and Monismith, S. G, *J. Fluid Mech.,* **354**, 175-208, 1998

[19] Moser, R. D. and Rogers, M. M., *Phys. Fluids*, A3(5), 1128-1134, 1991

[20] Harstad, K. and Bellan, J., *Int. J. Heat Mass Transfer,* **42,** 961-970, 1999

Time	$t^* = 100$		$t^* = 145$		$t^* = 170$	
	Unfiltered	Filtered	Unfiltered	Filtered	Unfiltered	Filtered
g_{vis}	1.54×10^7	1.15×10^7	1.61×10^7	1.20×10^7	1.39×10^7	1.04×10^7
g_{temp}	5.59×10^4	5.48×10^4	5.08×10^4	5.01×10^4	2.87×10^4	2.85×10^4
g_{mass}	3.17×10^5	2.42×10^5	3.22×10^5	2.50×10^5	2.18×10^5	1.53×10^5
g	1.58×10^7	1.18×10^7	1.64×10^7	1.23×10^7	1.43×10^7	1.06×10^7

Table 1: Average Entropy Production based on Unfiltered and Filtered Quantities

Time	$t^* = 100$		$t^* = 145$		$t^* = 170$	
	Unfiltered	Filtered	Unfiltered	Filtered	Unfiltered	Filtered
g_{vis}	4.11×10^7	2.85×10^7	3.74×10^7	2.62×10^7	3.24×10^7	2.18×10^7
g_{temp}	2.37×10^5	2.31×10^5	1.67×10^5	1.64×10^5	7.78×10^4	7.72×10^4
g_{mass}	1.73×10^6	9.09×10^5	9.80×10^5	6.99×10^5	1.63×10^6	3.41×10^5
g	4.21×10^7	2.93×10^7	3.82×10^7	2.68×10^7	3.28×10^7	2.21×10^7

Table 2: Root-Mean-Square Entropy Production based on Unfiltered and Filtered Quantities

Figure Captions

Figure 1. Momentum (——) and product ($\cdot\cdot\cdot\cdot$) thickness, enstrophy ($-\ -\ -$) and averaged positive spanwise vorticity ($-\ \cdot\ -\ \cdot\ -$) as a function of time.

Figure 2. Unfiltered (U) and filtered (F) plane averages of the various contributions to the averaged dissipation at $t^* = 100$ (2a), 145 (2b) and 170 (2c). g_{vis}U (——), g_{vis}F ($-\ -\ -$), g_{mass}U ($-\ \cdot\ -\ \cdot\ -$), g_{mass}F ($-\ \cdot\cdot\ -\ \cdot\cdot\ -$), g_{temp}U (—— ——), g_{temp}F ($\cdot\cdot\cdot\cdot$).

Figure 3. Unfiltered (U) and filtered (F) plane averages of the various contributions to the RMS dissipation at $t^* = 100$ (3a), 145 (3b) and 170 (3c). g_{vis}U (——), g_{vis}F ($-\ -\ -$), g_{mass}U ($-\ \cdot\ -\ \cdot\ -$), g_{mass}F ($-\ \cdot\cdot\ -\ \cdot\cdot\ -$), g_{temp}U (—— ——), g_{temp}F ($\cdot\cdot\cdot\cdot$).

Figure 4. Contours of the total unfiltered dissipation in the braid plane (a) and the magnitude of the density gradient in the braid plane (b) at $t^* = 170$.

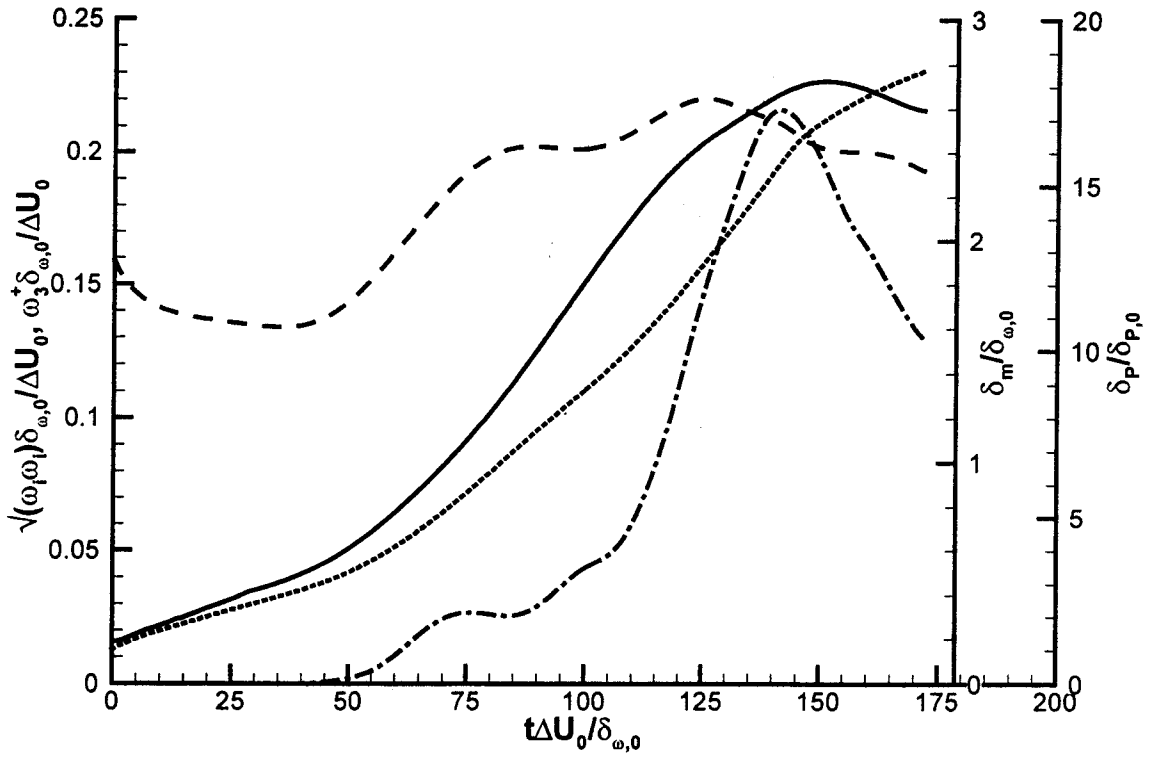
0.25
0.2
0.15
0.1
0.05
0
0
25
50
75
100
125
150
175
200
3
2
1
0
20
15
10
5
0
$\sqrt{(\omega_i\omega_j)}\delta_{\omega,0}/\Delta U_0$, $\omega_3^+\delta_{\omega,0}/\Delta U_0$
$t\Delta U_0/\delta_{\omega,0}$
$\delta_m/\delta_{\omega,0}$
$\delta_P/\delta_{P,0}$

fig 1

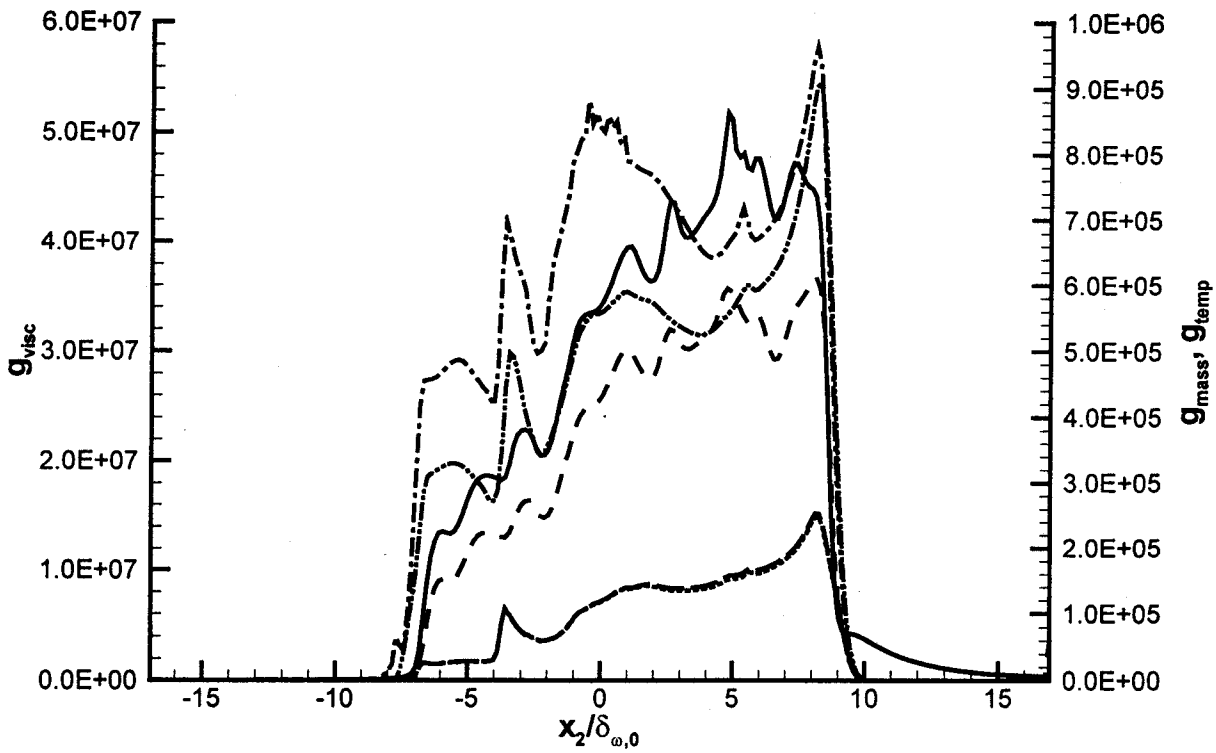
6.0E+07
5.0E+07
4.0E+07
3.0E+07
2.0E+07
1.0E+07
0.0E+00
g_{visc}
1.0E+06
9.0E+05
8.0E+05
7.0E+05
6.0E+05
5.0E+05
4.0E+05
3.0E+05
2.0E+05
1.0E+05
0.0E+00
g_{mass}, g_{temp}
-15
-10
-5
0
5
10
15
$x_2/\delta_{\omega,0}$

Fig 2a

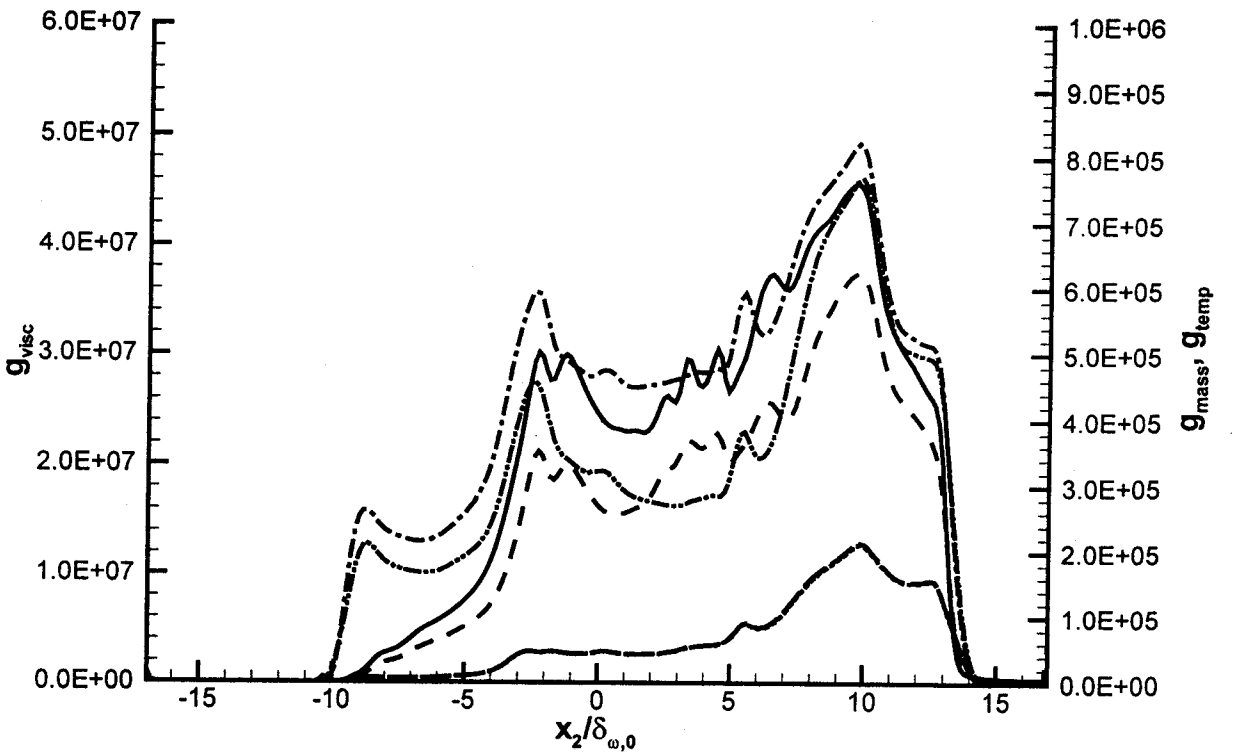
6.0E+07
5.0E+07
4.0E+07
3.0E+07
2.0E+07
1.0E+07
0.0E+00
g_{visc}
1.0E+06
9.0E+05
8.0E+05
7.0E+05
6.0E+05
5.0E+05
4.0E+05
3.0E+05
2.0E+05
1.0E+05
0.0E+00
g_{mass}, g_{temp}
-15
-10
-5
0
5
10
15
$x_2/\delta_{\omega,0}$

fig 26

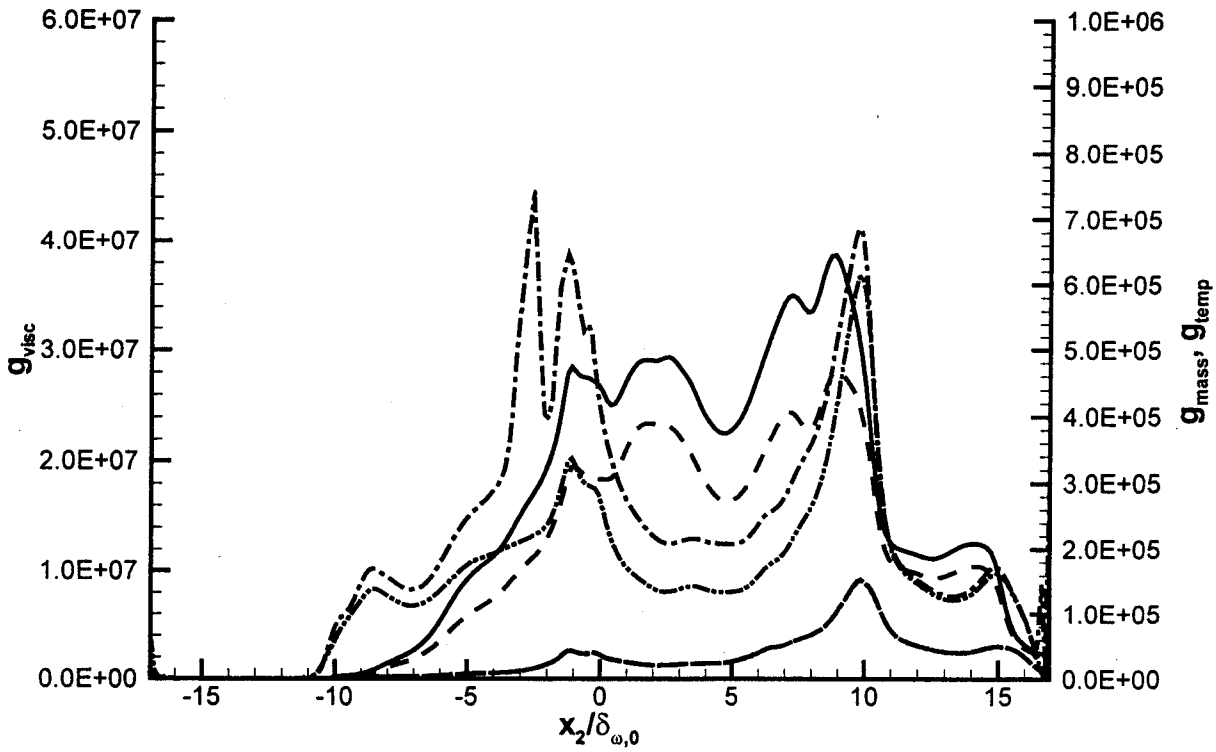
6.0E+07
5.0E+07
4.0E+07
3.0E+07
2.0E+07
1.0E+07
0.0E+00
g_{visc}
1.0E+06
9.0E+05
8.0E+05
7.0E+05
6.0E+05
5.0E+05
4.0E+05
3.0E+05
2.0E+05
1.0E+05
0.0E+00
g_{mass}, g_{temp}
-15
-10
-5
0
5
10
15
$x_2/\delta_{\omega,0}$

Fig 2c

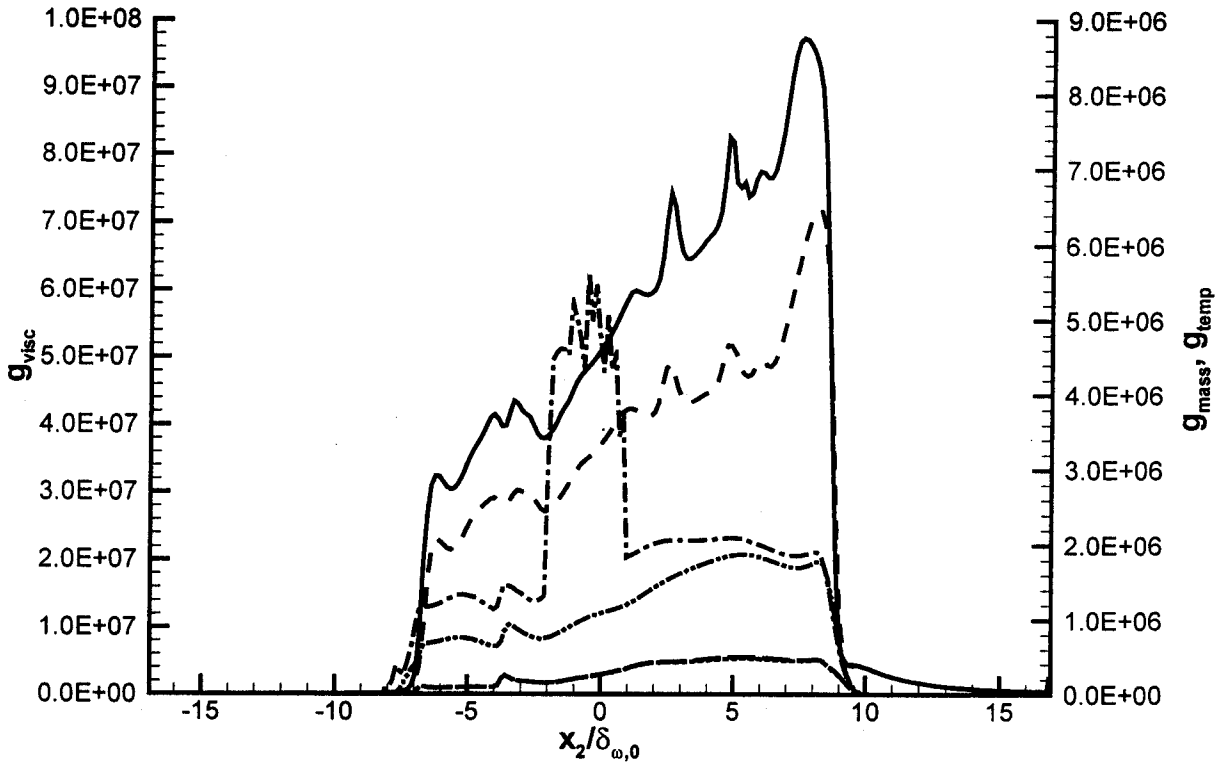
1.0E+08
9.0E+07
8.0E+07
7.0E+07
6.0E+07
5.0E+07
4.0E+07
3.0E+07
2.0E+07
1.0E+07
0.0E+00
g_{visc}
9.0E+06
8.0E+06
7.0E+06
6.0E+06
5.0E+06
4.0E+06
3.0E+06
2.0E+06
1.0E+06
0.0E+00
g_{mass}, g_{temp}
-15
-10
-5
0
5
10
15
$x_2/\delta_{\omega,0}$

Fig 3a

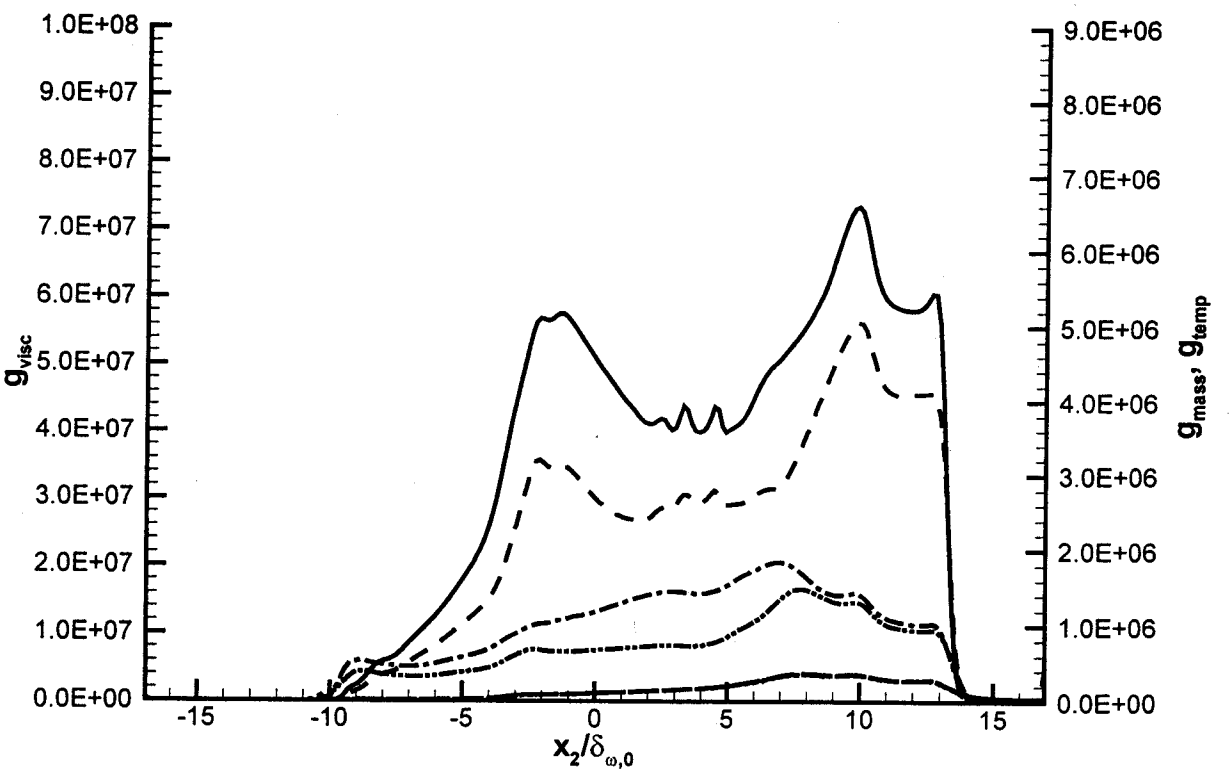
1.0E+08
9.0E+07
8.0E+07
7.0E+07
6.0E+07
5.0E+07
4.0E+07
3.0E+07
2.0E+07
1.0E+07
0.0E+00
g_{visc}
9.0E+06
8.0E+06
7.0E+06
6.0E+06
5.0E+06
4.0E+06
3.0E+06
2.0E+06
1.0E+06
0.0E+00
g_{mass}, g_{temp}
-15
-10
-5
0
5
10
15
$x_2/\delta_{\omega,0}$

Fig 36

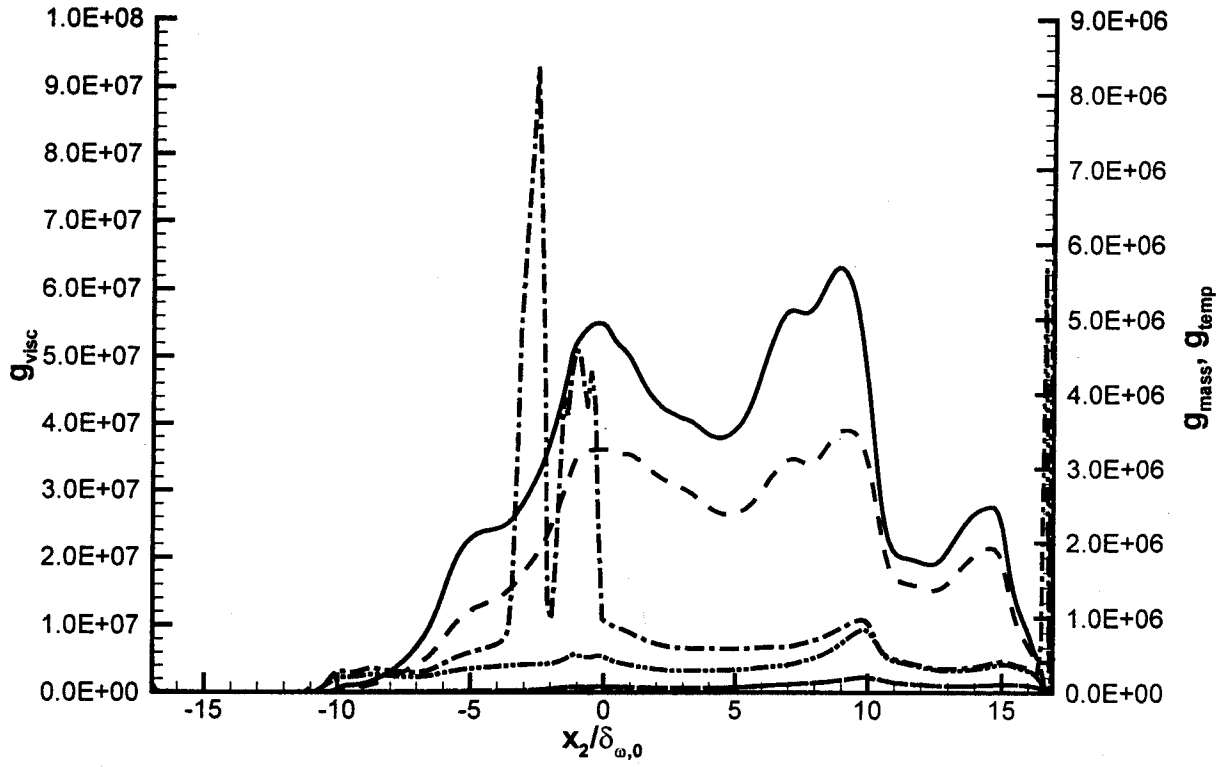
1.0E+08
9.0E+07
8.0E+07
7.0E+07
6.0E+07
5.0E+07
4.0E+07
3.0E+07
2.0E+07
1.0E+07
0.0E+00
g_{visc}
9.0E+06
8.0E+06
7.0E+06
6.0E+06
5.0E+06
4.0E+06
3.0E+06
2.0E+06
1.0E+06
0.0E+00
g_{mass}, g_{temp}
-15
-10
-5
0
5
10
15
$x_2/\delta_{\omega,0}$

Fig 3c

a)

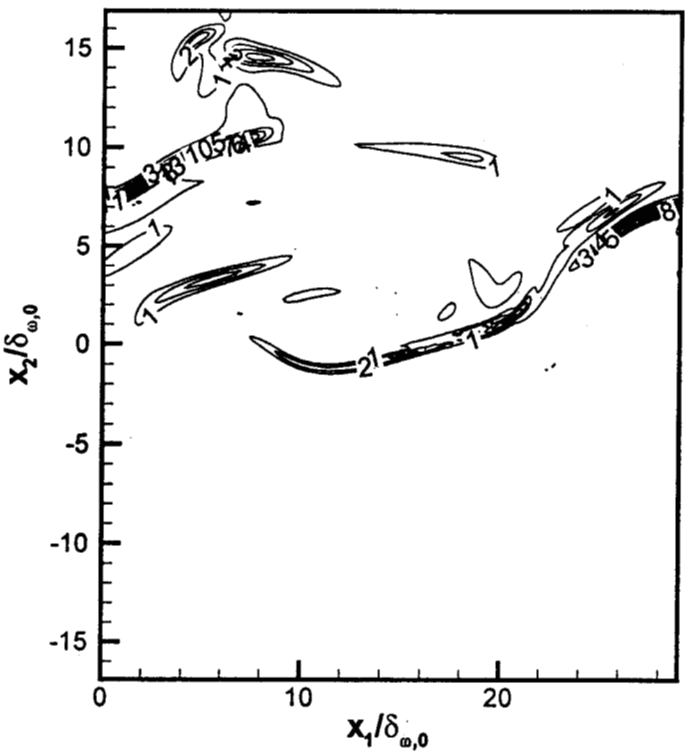

Level	g
15	4.60E+08
14	4.29E+08
13	3.98E+08
12	3.68E+08
11	3.37E+08
10	3.06E+08
9	2.76E+08
8	2.45E+08
7	2.15E+08
6	1.84E+08
5	1.53E+08
4	1.23E+08
3	9.19E+07
2	6.13E+07
1	3.06E+07

b)

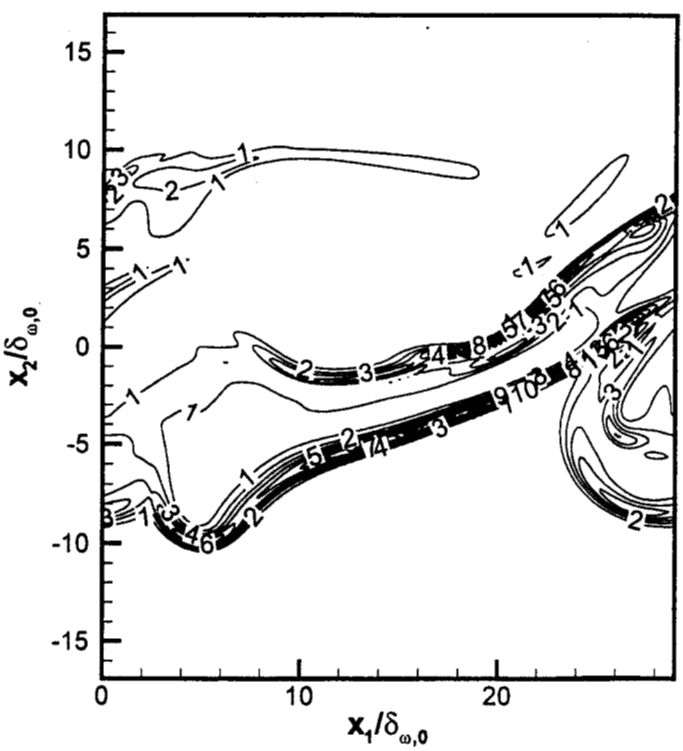

Level	$\lvert\nabla\rho\rvert$
15	9.24E+04
14	8.62E+04
13	8.01E+04
12	7.39E+04
11	6.78E+04
10	6.16E+04
9	5.54E+04
8	4.93E+04
7	4.31E+04
6	3.70E+04
5	3.08E+04
4	2.46E+04
3	1.85E+04
2	1.23E+04
1	6.16E+03

Fig 4